

# “Processing and characterization of textured ceramic layered architectures”

Report for the Austrian Marshall Plan Foundation

Author: Anna-Katharina Hofer

Supervisor MUL: Raul Bermejo

Supervisor PSU: Gary L. Messing

Leoben, März 2017

PennState



DEPARTMENT OF  
MATERIALS  
SCIENCE AND  
ENGINEERING  
COLLEGE OF EARTH AND  
MINERAL SCIENCES



<b>0. Abstract</b> .....	1
<b>1. Introduction</b> .....	1
1.1 Ceramics: properties and applications.....	1
1.2. Design strategies for improving mechanical behavior .....	3
<b>2. Experimental Work</b> .....	5
2.1. Materials of study and architectures.....	5
2.1.1. Monolithic materials.....	7
2.1.1.1. Textured Alumina.....	7
2.1.2. Layered architectures.....	7
2.2. Processing of monoliths and laminates .....	10
2.2.1 Selection of powders .....	10
2.2.2 Stability of colloidal suspensions .....	11
2.2.3 Binder systems.....	13
2.2.4. Preparation of the slurries.....	14
2.2.5. Tape Casting.....	17
2.2.6. Hot Pressing (HP) & Lamination (IP) .....	18
2.2.7. Binder Burn Out (BB-Out).....	18
2.2.8. Cold Isostatic Pressing .....	20
2.2.9. Sintering .....	20
<b>3. Results and discussion</b> .....	22
3.1. Selection of binder system.....	22
3.2. Dimensions and shrinkage of monolithic and layered samples.....	23
3.3. Density measurements.....	25
3.4. Microstructural characterization.....	26
3.4.1. Sample preparation.....	26
3.4.2. Optical and scanning electron microscopy (SEM) .....	26
3.4.3. Degree of texture through X-Ray analysis .....	28
<b>4. Future work</b> .....	31
<b>References</b> .....	33

## **0. Abstract**

The project was carried out at the Department of Materials Science and Engineering at The Pennsylvania State University (PSU), USA, and had a total duration of 3.5 months. The performed research is part of a more extensive scientific program between the Montanuniversitaet and Penn State University, aiming to explore the scientific principles that can be utilized to obtain “flaw tolerant” and crack-resistant ceramics for use in structural and functional applications. During the internship at PSU, the research agenda was focussed on the design and fabrication of textured layered ceramic architectures. Different layered structures were processed using tape-casting technology combining layers with different geometry, compositions and properties, i.e. thickness, location, material microstructure (e.g. equiaxial or textured).

## **1. Introduction**

### **1.1 Ceramics: properties and applications**

The interest for the mechanical behavior of ceramic materials has been always motivated by the in-service demands made on structural components and machine parts which often require the application of brittle materials, particularly ceramics and glasses, because of certain outstanding properties such as high-temperature stability, oxidation and corrosion resistance, dimensional stability, hardness and wear resistance, as well as other special ones such as thermal, electrical or optical properties. Some examples are high temperature resistant parts for metallurgical processes, wear-resistant plates for paper machines, accurate position holders for optics, resistors and capacitors in microelectronic packages, piezo-ceramic controlled valves for engines, electrolytes in electrochemical solid oxide fuel cells and hard, bio-inert implants in medicine.

A limitation for the use of ceramics is their low fracture toughness, which often causes spontaneous brittle failure of the component or system. Contrary to metals, crack propagation in brittle materials such as ceramics is usually catastrophic, due to the lack of plastic deformation. The brittle fracture of glasses and ceramics is a consequence of the material defects located within the bulk and especially at the surface, resulting from the processing and/or machining procedures as well as from damage in service [1, 2]. The distribution of defects of different sizes within a ceramic component yields a statistically variable strength which can be described, in

many cases, by the Weibull theory [3, 4]. As a consequence of such behavior, there remains a (small) probability of failure even at very small applied loads (i.e. no lower bound for strength). Since flaws are intrinsic to processing and in most cases unavoidable, the mechanical strength and reliability of ceramic components is associated with the flaw distribution in the material. This scatter in strength affects the reliability and lifetime of ceramics, thus limiting the market potential and in some cases hindering the development of completely new markets for ceramic devices.

For next generation devices it is necessary to combine materials (ceramic, metals and polymers) that can bring new functionality to components, creating so-called hybrid planar systems. Tape casting technology has enabled the fabrication of such hybrid devices based on a “multilayer architectural design” [5, 6]. Some examples of such advanced engineering systems are (i) planar Solid Oxide Fuel Cells (SOFC), (ii) stacked piezo-actuators and sensor devices, and (iii) conducting plates for wireless communications (see example in **Fig. 1**).

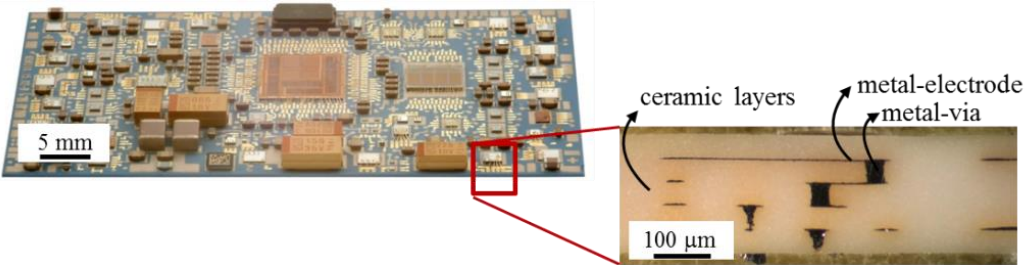


**Figure 1.** Microelectronic functional system with mounted ceramic components. A cross-section of the ceramic printed circuit board substrate shows the combination of ceramic layers and metallization in a 3D multilayer architecture.

However, the fabrication of components having two or more different materials can be a challenge from the structural viewpoint. The different thermal expansion coefficients and elastic properties of the combined materials can generate significant “residual stresses” in some of the parts (e.g. in the ceramic layers). While compressive residual stresses can be beneficial in strengthening the material (e.g. Gorilla® glass), tensile residual stresses may lead to the initiation and/or propagation of cracks (e.g. surface cracks) from starting defects, even before service loading conditions.

Novel concepts are still needed to build tougher and more reliable ceramic materials that can be employed in both structural and functional ceramic-based systems. As a matter of fact, the layer-wise architecture of hybrid planar devices offers unique opportunities for tailoring the internal stress fields and the microstructure in the materials to mitigate crack propagation and thus produce “flaw tolerant” and crack-resistant devices.

## **1.2. Design strategies for improving mechanical behavior**

In recent years, thanks to the remarkable progress in terms of microstructural design and advanced processing (e.g. colloidal processing) [7-10], the mechanical strength in ceramics has been increased as well as the variability in strength significantly reduced. A successful application of microstructural engineering has been demonstrated for instance on “textured” ceramic materials, where the individual grains are grown and oriented in a particular direction, seeking either to increase the mechanical properties (e.g. strength and toughness) and/or enhance functionality (e.g. dielectric constant, piezo response, etc) [11]. Texturing alumina ceramics, for instance, has been mainly driven by the so-called “templated grain growth” (TGG) technique, as developed at The Pennsylvania State University by the group of Prof. G.L. Messing [12]. In TGG processing a subset of template particles is uniformly distributed in a fine powder and the templates are aligned during forming, for instance under a doctor blade during tape casting or during uniaxial pressing. After densification, the oriented template grains grow preferentially with further heating by consuming the non-oriented matrix grains and, as a result, the final microstructure consists of grains with an orientation distribution that is determined (or templated) by the initial placement and alignment of the template particles (see **Fig. 2**). For successful TGG processing the template particles must be larger than the matrix particles (preferably at least ten times larger) because the size difference is the driving force for preferred growth [14]. The template particles also have a large aspect ratio because most TGG forming processes use shear stresses for template alignment.

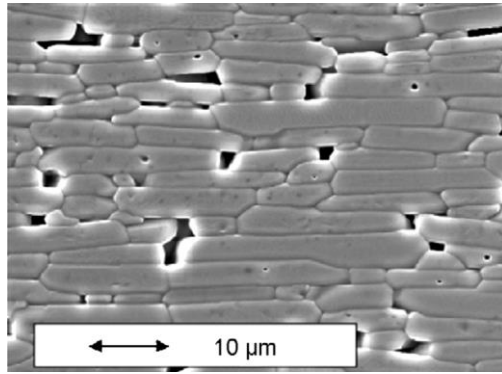


**Figure 2.** SEM micrograph of a TGG textured alumina with 2% ( $\text{SiO}_2 + \text{CaO}$ ) dopant and 15 vol% template loading [13].

As an extension of this “oriented” platelet-like microstructural concept, multilayer designs have also been attempted in many ways aiming to improve both the resistance to crack propagation and the mechanical reliability of ceramic components [15-24]. Composite materials using symmetric multilayer architectures (e.g. ceramic composites such as alumina-zirconia and mullite-alumina among others) have been reported to exhibit increased fracture toughness, higher energy absorption capability and/or non-catastrophic fracture behavior compared to their constituent (monolithic) materials. Among the various laminate designs reported in the literature, two main approaches regarding the fracture energy of the layer interfaces must be highlighted, i.e. the use of “weak” or “strong” interfaces between the layers. A particular case of the latter is based on the capability of inducing residual stresses in the layers during cooling from sintering.

Ceramic-ceramic layered composites have proven to be effective by introducing internal compressive residual stresses in embedded layers, in order to provide a barrier to crack propagation and, in some cases, even stop the propagation of cracks (see for instance **Fig. 3**). As a result, a lower bound for the material strength can be defined (so-called threshold strength), below which failure does not occur, thus increasing reliability [19, 25-27]. Recent work of the team supporting this work has shed light on the benefits of combining residual stresses with microstructural features [28]. However, the potential of building composites with embedded “protective” features having a tailored microstructure to obtain reliable ceramic components or systems has not been sufficiently explored yet.

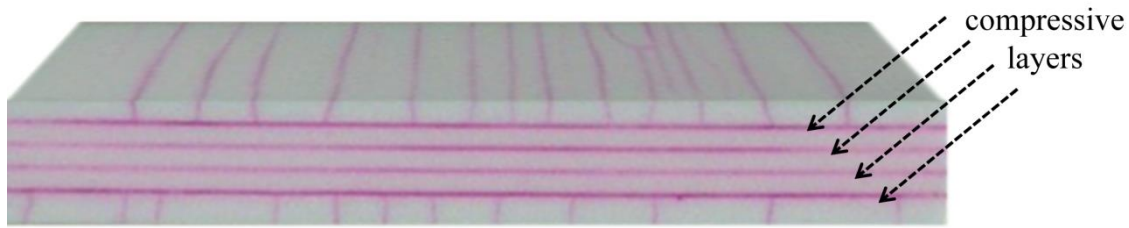


**Figure 3:** Surface cracks arrested at the “embedded” compressive layers of a nine-layered  $\text{Al}_2\text{O}_3\text{-ZrO}_2$  ceramic, during a thermal shock test in water [29]. Cracks are highlighted by a red color.

The overarching aim of the internship at the host institution was to design and fabricate novel ceramic composite architectures, consisting of combination of two materials having tailored microstructures (*e.g.* texture) in a layered architecture. The main effort was put on the processing and design optimization of architectures. In the following, the experimental work will be presented.

## 2. Experimental Work

### 2.1. Materials of study and architectures

There is a wide variety of advanced ceramics for structural applications, which can be classified in oxide and non-oxide systems. The former are for example Aluminium oxide (=Alumina,  $\text{Al}_2\text{O}_3$ ), Zirconium dioxide (=Zirconia,  $\text{ZrO}_2$ ), Magnesium oxide (Magnesia,  $\text{MgO}$ ) or Titan(IV)-oxide (Titania,  $\text{TiO}_2$ ). These inorganic compounds mainly consist of ionic bonds. Non-oxide ceramics are for instance Silicon nitride ( $\text{Si}_3\text{N}_4$ ), Silicon carbide ( $\text{SiC}$ ) or Aluminium nitride ( $\text{AlN}$ ), holding more covalent bonds rather than ionic bonds, which results in much higher bond energies than for oxide ceramics.

Among the different ceramics, alumina, zirconia and alumina-zirconia composites (*i.e.* a combination of both materials) were selected for this study.

For technical ceramic applications alumina is employed to 80%. It is extracted from Bauxite via the Bayer-Process and can exist as different phases (*e.g.*  $\gamma$  (cubic),  $\theta$  (monoclinic)). The most common is the  $\alpha$ -phase, also called corundum, which has a rhombohedral crystal structure. This structure is built through large oxygen ions (anions), showing a formation of a hexagonal close packed array. Two thirds (for charge neutrality maintenance) of the octahedral sites of this hexagonal array are filled with Aluminium ions (cations) (see **Fig. 4**). [30]

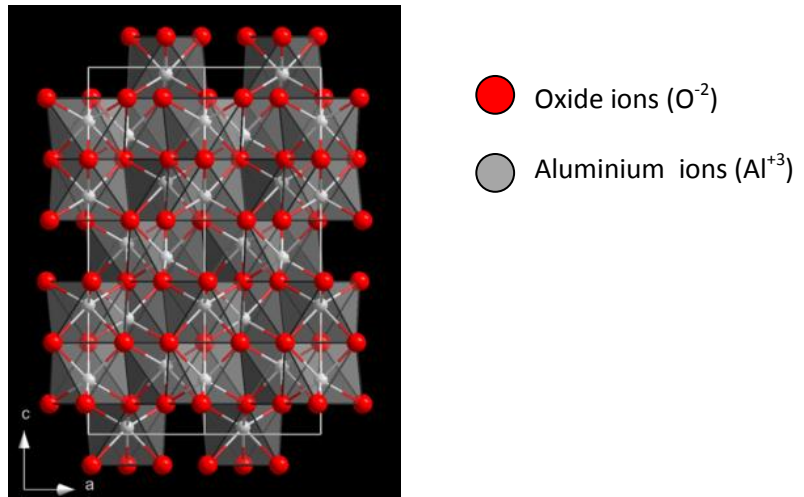


**Figure 4:** crystal structure of Aluminium oxide ( $Al_2O_3$ ) [31]

Zirconia actually occurs in a monoclinic crystal structure at room temperature. At a temperature of about  $1170\text{ }^\circ\text{C}$  it transforms into a tetragonal and at  $\sim 2370\text{ }^\circ\text{C}$  into a cubic phase. Due to the martensitic transformation from the cubic phase to the tetragonal, higher toughness than in the monoclinic phase can be achieved. However, the temperature at which tetragonal zirconia is stable is  $\sim 1170\text{ }^\circ\text{C}$ , therefore Yttriumoxide ( $Y_2O_3$ ) is used to stabilize this phase at room temperature. Yttrium ions occupy positions of  $Zr^{4+}$  ions and as a result induce vacancies of oxygen (see **Fig. 5**).[32]

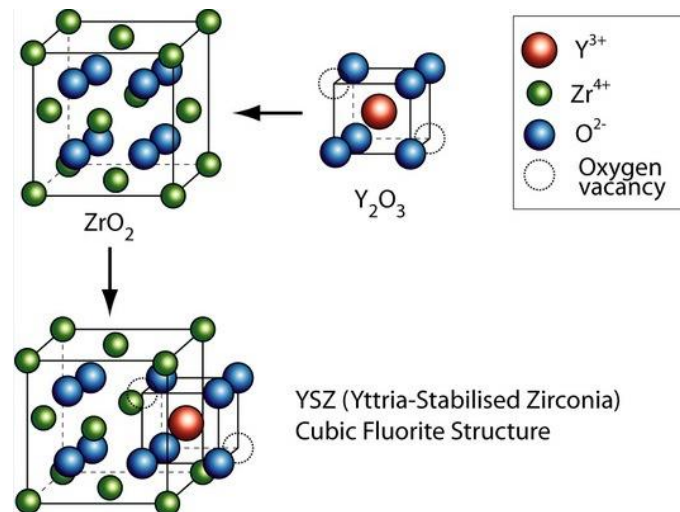


**Figure 5:** process of doping  $ZrO_2$  with  $Y_2O_3$  to stabilize the tetragonal phase [33]

### 2.1.1. Monolithic materials

Monolithic samples were fabricated to determine mechanical and thermal properties of the main materials (textured alumina and non-textured alumina (with  $ZrO_2$ )) in later work.

#### *2.1.1.1. Textured Alumina*

Textured materials can be fabricated using different techniques, for example uniaxial pressing during the sintering process or for metallic materials applying a metallic field for particle orientation. Though, in this study as already briefly mentioned in the introduction Templated Grain Growth (TGG) was applied to achieve a certain orientation of the alumina grains. Here 95% of the solids was alumina powder (particle size  $\sim 0.20 \mu\text{m}$ ) and 5% alumina templates, which are platelets having a flake like shape (diameter  $\sim 3 \mu\text{m}$ , thickness  $\sim 0.10 \mu\text{m}$ ). [28]

See **Table 2** for the desired sintered dimensions and the correlated green part dimensions.

#### *2.1.1.2. Non-Textured (Equiaxed) Alumina*

In contrast to the textured alumina, non-textured alumina shows an equiaxial microstructure, meaning that the grains do not show any preferential orientation. In the equiaxed material it was required to have small grain sizes, due to the improvement of mechanical properties and the result of a better interface between non-textured and textured materials for the layered architectures. To obtain small grain sizes in alumina, it was doped with 5% of yttrium stabilized zirconia. Moreover, zirconia increases the coefficient of thermal expansion of alumina (as investigated in previous work [28]), see coefficients of thermal expansion in **Tab. 1**.

All the dimensions of the sintered and green stage parts are also listed in **Tab. 2**.

**Table 1:** coefficients of thermal expansion of  $Al_2O_3$  and  $ZrO_2$  [30,32]

$\alpha (Al_2O_3)$	$*10^{-6} K^{-1}$	5.43
$\alpha (ZrO_2)$	$*10^{-6} K^{-1}$	10.00

### 2.1.2. Layered architectures

For the layered architectures, textured and non-textured materials were combined in different designs. To compare the effect of different thicknesses in the samples (especially the effect of outer layers) on the mechanical properties three designs were fabricated. It must be highlighted that the volume ratio between the textured ( $V_T$ ) and non-textured ( $V_{NT}$ ) materials was fixed to  $V_T/V_{NT} = 1/6$  for all designs. This volume ratio is due to calculations taking the emerging residual stresses in the layers into account, leading to an improvement of the fracture behavior, as it will be described in more detail in section 3.

Fundamentally it was distinguished between periodic (P) and non-periodic (NP) designs. The periodic samples (P) consisted of 9 layers in total, alternating non-textured and textured

material, where non-textured (equiaxed) material formed the outer most layers. In comparison the non-periodic samples were built in 5 layers, where the outer equiaxed material had a much lower thickness compared to the second (textured) layer. The middle layer showed a very high thickness, to fulfill the volume ratio of 1:6. For the non-periodic design two different architectures, differing in the thicknesses of the outer most and second layer, were fabricated (referred to as NP1 and NP2).

Figure 6 shows the two different main designs of periodic (**Fig. 6a**) and non-periodic (**Fig. 6b**) architectures. The layers colored in blue, display the non-textured material, where the white arrows indicate the presence of in-plane (i.e. parallel to the layer plane) residual tensile stresses, occurring due to the different thermal expansion of the various materials. In contrast, the yellow colored layers, illustrating the textured material, show residual compressive stresses, indicated by the red arrows.

In **Table 2** all the desired dimensions of the final sintered samples and the dimensions of the green parts are given, calculated considering the shrinkage of the monolithic samples.

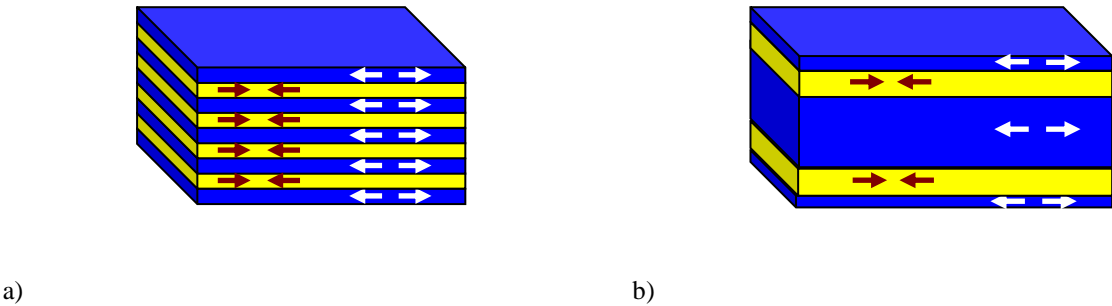


**Figure 6:** Schematic of **a)** Periodic design (9 layers), **b)** non-periodic design (5 layers)

**Table 2:** dimensions of monolithic and laminated samples in the green stage and the sintered stage, considering the shrinkage during processing<sup>1</sup>

			green dimensions	desired dimensions (after sintering)	shrinkage
			[ $\mu\text{m}$ ]	[ $\mu\text{m}$ ]	[%]
Textured Alumina (TA)	layer	1	3.86	3	-22.35
Equiaxed Alumina (EA)	layer	1	3.71	3	-19.19
Periodic (P)	layer	1	485	360	-25.77
		2	90	75	-16.67
		3	485	360	-25.77
		4	90	75	-16.67
		5	485	360	-25.77
		6	90	75	-16.67
		7	485	360	-25.77
		8	90	75	-16.67
		9	485	360	-25.77
Non-Periodic: design 1 (NP1)	layer	1	80	50	-37.50
		2	200	150	-25.00
		3	2240	1700	-24.11
		4	200	150	-25.00
		5	80	50	-37.50
Non-Periodic: design 2 (NP2)	layer	1	80	50	-37.50
		2	333	250	-25.00
		3	3800	2900	-23.68
		4	333	250	-25.00
		5	80	50	-37.50

<sup>1</sup>all the data are **estimated values**; due to the different materials, thermal expansion of these and different thicknesses in NP, the shrinkage in the laminates can not only be predicted by considering the shrinkage of the monolithic parts;

## 2.2. Processing of monoliths and laminates

Among the different processing approaches to conform ceramic materials, “colloidal processing” was selected for this investigation, which is generally defined as the processing of ceramic powders in the colloidal size range, i.e. from 1 to  $10^3$  nm [34]. One of the advantages of using starting “colloids” is to achieve a better control of raw materials and processing conditions, thus limiting heterogeneities in the microstructure. The processing route employed in this study to fabricate the samples was “tape casting” [35].

In a first stage, monolithic samples were fabricated to be used as reference materials. Two types of microstructures were aimed: (i) *textured* and (ii) *non-textured*, regarding the degree of preferred orientation of the crystals in the microstructure (with respect to the casting direction). Special effort was put on the optimization of the so-called templated grain growth (TGG) process to *texture* the materials under consideration. In a second step, layered architectures combining textured and non-textured layered materials were fabricated. In this regard, two different configurations were attempted: (a) periodic and (b) non-periodic, indicating the distribution of the “embedded” layers within the multilayer structure (see section 2.1 for more details).

The tape casting process, as conducted in this investigation, consisted of the following steps: (i) selection of powders and binder system, (ii) preparation of the slurries, (iii) casting of slurries, (iv) hot pressing and lamination, (v) binder burn-out, (vi) cold isostatic pressing, and (vii) sintering.

### 2.2.1 Selection of powders

For the fabrication of the monolithic (textured and non-textured) and the layered samples three kinds of powder were applied. The main powder, which formed the matrix of all the samples fabricated was the  $\alpha$ -Alumina powder (AKP-50, Sumitomo Chemicals, Tokyo, Japan). This powder has a  $D_{v50}$  (50% of particles have a particle size below this dimension) is  $0.204\ \mu\text{m}$ , and a range of particle sizes from  $0.086\ \mu\text{m}$  to  $0.345\ \mu\text{m}$ . For the textured samples templates were added to obtain templated grain growth. These  $\alpha$ - $\text{Al}_2\text{O}_3$  templates (Rona Flair® White Sapphire, EMD Performance Materials Corp., Darmstadt, Deutschland) had a thickness of  $\sim 0.10\ \mu\text{m}$  and a diameter of  $\sim 3\ \mu\text{m}$ . The third powder was only applied to the non-textured material, yttria-stabilized zirconia powder (TZ-3Y, Tosoh, Tokyo, Japan) with a particle size of  $0.60\ \mu\text{m}$ .

### 2.2.2 Stability of colloidal suspensions

In colloidal suspensions the powders experience repulsive and attractive (Van der Waals) forces when they are moving (kinetic energy). Depending on the particle size the repulsive forces increase with the third power of the particle diameter. In comparison to that the Van der Waals forces increase linear. According to this for small particles the ratio of Van der Waals forces is much more dominant than the repulsive forces. To ensure a stable colloidal suspension the Zeta-Potential has to be measured. [34]

The model of the electric double layer at an ionically charged surface can describe the Zeta-Potential, after the DLVO theory (Derjagin, Landau, Verwey and Overbeek), see **Fig. 7**. In this model the ionically charged surface of a particle is surrounded by a first layer of ions with opposite charge as the ions on the surface of the particle, called the Stern layer. Around this layer again, the Diffuse layer or also called the Gouy-Chapman layer is formed, containing negative as well as positive charged ions. The potential between these two layers, Stern and Diffuse layer, is the Zeta-Potential, which can be measured by moving either the particle or the liquid, in which the particles are dispersed. This movement causes a shift of the potential, which indicates the size of the ionic cloud and the Zeta-Potential.

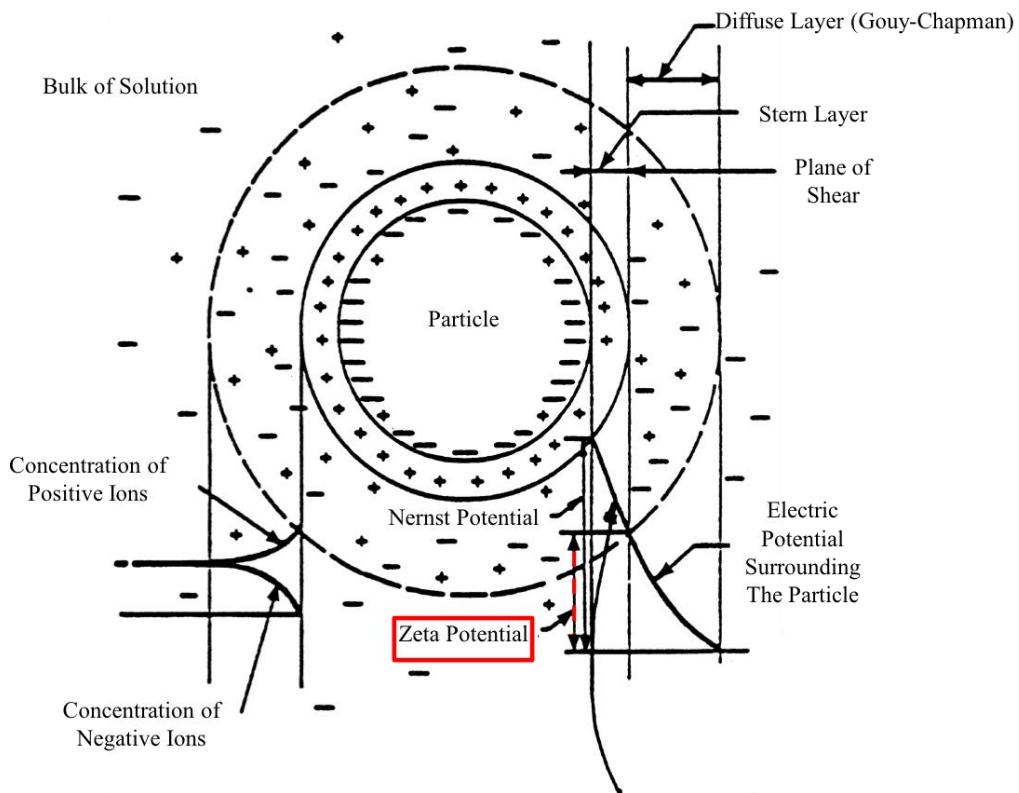


**Figure 7:** Double layer model after DLVO [36]

Any material has a certain Isoelectric Point (IEP), which is the pH of a solution at which the Zeta-Potential becomes zero, changing its polarity. At this point the suspension is totally unstable, instantaneous flocculation occurs. To obtain a well dispersed stable suspension the pH should be at least four pH units either below or above the IEP, measured from the original pH of the material, see **Fig. 8**. [36]

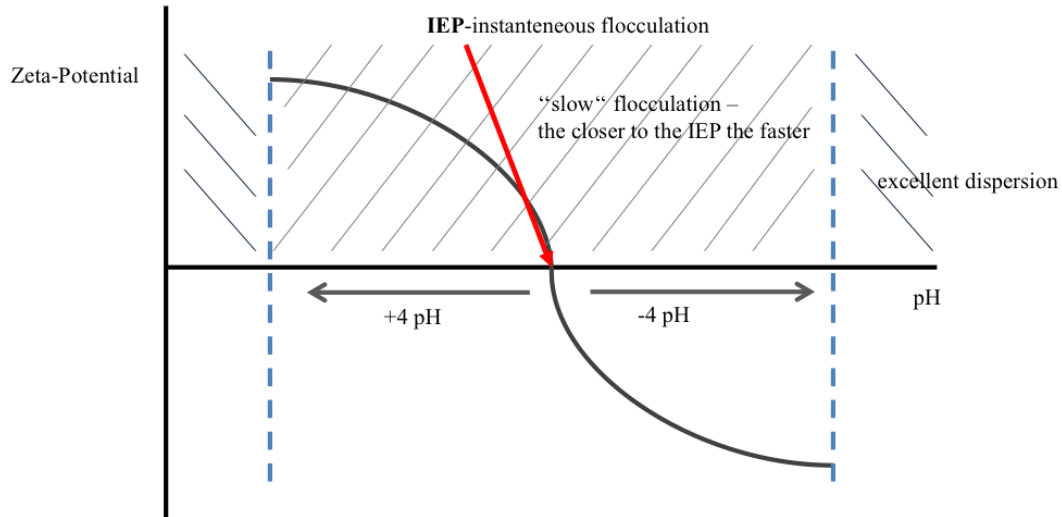


**Figure 8:** schematic of a Zeta-Potential – pH curve showing stable and unstable regions of a dispersion

As a result an important factor that has to be considered for the right selection of the binder system for the formulation of the ceramic slurry is the value of the pH from the binder as well as from the ceramic material. If the values of the two different components are more than about two pH units apart, flocculation or settling of the particles can occur. Flocculation is due to the change of the Zeta-Potential closer to the IEP of the ceramic material by adding a binder with a much different pH value. For alumina the pH value is 9.5, meaning the pH should not be higher than 11.5 or lower than 7.5 after adding the binder. Otherwise flocculation or settling of the particles can occur, at lower pH values, or the alumina particles start to dissolve if the pH gets too high.

### 2.2.3 Binder systems

For most fabrications of ceramic materials a binder is needed in the forming process. A binder obtains the ability of handling a ceramic material before sintering without fracture (cracking). Binders are polymers solved either in an aqueous or a non-aqueous liquid. It surrounds and holds the ceramic powder particles together via capillarity forces. For the appropriate selection of the binder, the ceramic powder has to be “wetable” by the binder. This means a contact angle ( $\theta$ ) below  $90^\circ$  between the solid and the liquid surface, see **Fig. 9**. This condition must be given to obtain well dispersed particles in the slurry.

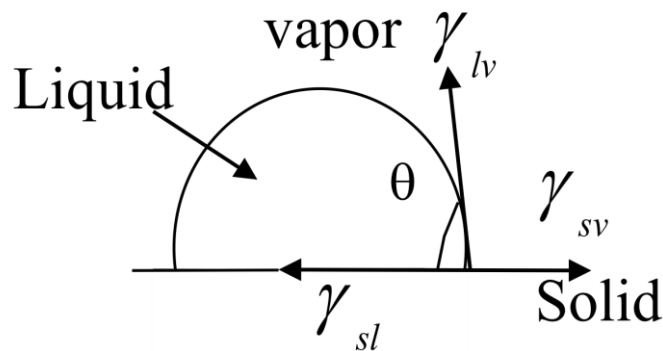


**Figure 9:** Schematic for describing the contact angle ( $\theta$ ), which should be  $<90^\circ$  for good wettability [36]

Besides the polymers of the binder, also other organic components are added, to achieve a better colloidal dispersion. Usually an additional dispersant is added, where the polymer-chains stabilize the particles, to avoid a direct contact between two particle surfaces. Another component which is commonly added is the plasticizer, which lowers the glass transition temperature of the polymer used as binder, to make it more flexible. To ensure that the resulting slurry does not contain too much air a defoamer is also added with the other components.

*PVA binder system:* First the polymer Polyvinylalcohol (PVA) (MW 85,000-124,000, Aldrich Chemistry, Steinheim, Deutschland) was used as organic binder. PVA is soluble in water, meaning here an aqueous system was used. Besides water, to solve the polymer binder, other components were also added, Polyethylene Glycol (PEG 600, Alfa Aesar, Ward Hill, MA, USA) as plasticizer, Duramax (Rohm&Haas inc., Rancho Dominguez, CA, USA) as dispersant and Surfynol (Air Products&Chemicals, Allentown, PA, USA) as defoamer.

*Acrylic binder system:* This new binder system now had to be applied to alumina powder material which was used. Meaning that the pH had to be measured, to ensure the pH of the alumina will still be stable after adding the organic components, and the right formulation of components had to be figured out. The acrylic binder system contained a water based binder (WB4101), a plasticizer (PL008), a dispersant (DS001) and a defoamer (DF002) (Polymer Innovations Inc., Vista, CA, USA).

#### 2.2.4. Preparation of the slurries

In the following three different preparation procedures for the slurries will be described.

First the preparation of a slurry for textured samples using the PVA binder system, second also for textured samples, but with the Acrylic binder system and last the preparation of a slurry for equiaxed samples with the Acrylic binder system and zirconia as dopant.

To obtain templated grain growth and as a result a textured structure, a liquid phase has to be present during the sintering process. Therefore the dopants CaO ( Ca(NO<sub>3</sub>)<sub>2</sub>, BDH Chemicals, Radnor, PA, USA) and SiO<sub>2</sub> (Aerosil 200) are added to the slurries for textured samples, which form the liquid phase during sintering. The ratio of CaO : SiO<sub>2</sub> = 1 : 1, and the experimentally analyzed ideal amount of these dopants is 0.25wt% of the total amount of ceramic material. Here CaO was added in form of Ca(NO<sub>3</sub>)<sub>2</sub>\*4H<sub>2</sub>O after dissolving it in 5 ml of DI-H<sub>2</sub>O. [28]

##### *a) Preparation of the slurry with the PVA binder system for textured samples:*

For this slurry the binder system had to be prepared first; for a detailed formulation refer to **Tab. 3a**). The PVA was dissolved in DI-H<sub>2</sub>O under permanent stirring on a stir plate at a temperature of 80°C. After about eight hours the PVA should be totally dissolved, no particles should be visible in the solution, and the other organic components, PEG, Duramax and Surfynol can be added. When the temperature of the binder solution had reached about room temperature, the organics, the ceramic powder and the dopants, Ca(NO<sub>3</sub>)<sub>2</sub>\*4H<sub>2</sub>O and SiO<sub>2</sub> were put together into a ball mill bottle. This bottle was filled to one third with 5 mm diameter alumina (Al<sub>2</sub>O<sub>3</sub>) beads. Too big beads can cause the breakage of particles to smaller sizes which can result in agglomeration. After 24 h of milling on ball mill, the alumina platelets are added to the bottle and ball milled for 1 h. Milling of the slurry with the added platelets for longer than one hour could lead to breakage of the platelets and loss of their actual purpose of being templates for the templated grain growth (TGG). After removing the bottle from the ball mill the slurry is sieved into a beaker and stirred for another 24 h to deair the slurry. To ensure that there are no more

bubbles in the slurry, it was put into vacuum executor for about 30 minutes and on the vibratory table.

*b) Preparation of the slurry with the Acrylic binder system for textured samples:*

Due to the formulation as listed in **Tab. 3b)** the acrylic binder components were mixed together in a beaker and stirred on a stir plate. After 30 minutes the dopants  $\text{Ca}(\text{NO}_3)_2 \cdot 4\text{H}_2\text{O}$  and  $\text{SiO}_2$  were added and mixed with the binder system for 1 h. Following the alumina powder was weighted into the ball mill bottle, as in a) this bottle was filled to 1/3 with 5 mm in diameter  $\text{Al}_2\text{O}_3$  beads, and additionally the stirred binder and dopants were added.

This slurry was mixed on the ball mill for 24 h, then after adding the  $\text{Al}_2\text{O}_3$  platelets another 30 minutes. After milling, the slurry was sieved in a beaker and stirred for at least 24 h to remove the trapped air. The beaker with the slurry was put in a vacuum executor for 10 min and on a vibratory table for about 5 minutes to ensure that the slurry is totally desired. In comparison to the PVA binder system the slurry with the acrylic binder must not be under vacuum longer than 10 min, otherwise it might induce more bubbles instead.

*c) Preparation of the slurry with the Acrylic binder system for non-textured samples:*

As described in b) the organic components of the acrylic binder system (see **Tab. 3c)**) were stirred in a beaker for 30 min first. For non-textured samples no liquid-phase is necessary during the sintering process, therefore no dopants had to be added in this preparation. The binder system and the ceramic powders, alumina and zirconia were then mixed together in the ball mill bottle and milled for 24 h. After milling and sieving the slurry into a beaker the slurry was stirred for 24 h, as already explained in a) and b) to remove the trapped air. To ensure an air-free slurry, it was put into the vacuum executor for 10 min and on the vibratory table for 5 min.

**Table 3:** Formulation of slurries for textured and non-textured samples

<b>a) Slurry with PVA binder for textured samples</b>			
Alumina powder	70.0394vol%	Organic binder	
Organic binder solution	26.3570vol%	DI-H <sub>2</sub> O	84.45vol%
		PVA	6.22vol%
		PEG	6.22vol%
		Duramax	2.22vol%
		Surfynol	0.89vol%
Ca(NO <sub>3</sub> ) <sub>2</sub> *4H <sub>2</sub> O	0.0899vol%		
SiO <sub>2</sub>	0.0225vol%		
Al <sub>2</sub> O <sub>3</sub> platelets	3.4912vol%		
<b>b) Slurry with Acrylic binder for textured samples</b>			
Alumina powder	82.5034vol%	Acrylic binder	
Acrylic binder solution	13.0158vol%	DI-H <sub>2</sub> O	48.98vol%
		WB4101	43.90vol%
		PL008	3.91vol%
		DS001	2.55vol%
		DF002	0.66vol%
Ca(NO <sub>3</sub> ) <sub>2</sub> *4H <sub>2</sub> O	0.1108vol%		
SiO <sub>2</sub>	0.0281vol%		
Al <sub>2</sub> O <sub>3</sub> platelets	4.3419vol%		
<b>c) Slurry with Acrylic binder for non-textured samples</b>			
Alumina powder	76.87vol%	Acrylic binder	
Acrylic binder solution	14.84%	DI-H <sub>2</sub> O	54.31vol%
		WB4101	41.33vol%
		PL008	3.74vol%
		DF002	0.62vol%
Zirconia	8.29vol%		

### 2.2.5. Tape Casting

Tape Casting of ceramic materials is a forming process to fabricate tapes with thicknesses of 25-1000  $\mu\text{m}$ . The operating mode of tape casting is that the slurry is poured into a fixed doctor blade. This doctor blade is put on a polymer foil, which is pulled from one side of the machine to the other one. Between the foil and the blade there is a gap, through which the slurry can run on the foil while it is pulled. The gap-height was 254 $\mu\text{m}$ , which was adjusted with a metallic lamella that had the required thickness.

The foil that was used for tape casting was a mylar (polymer sheet) material which had one non-coated side and one side coated with Silicon. For the tape casting of the alumina slurry with the components described earlier the non-coated side was used. Otherwise, the effect of non-wetting would have occurred and an incoherent tape would have resulted, see **Fig. 10a**).

After filling the doctor blade with the slurry the machine was run with a constant speed of 20% of the motor speed that correlates to a velocity of 0.801 cm/s. The setting of the motor speed, and thus of the velocity, depends on the viscosity of the slurry; the higher the viscosity the higher the velocity of pulling the mylar.

The casted tape was then dried in air for 24 h, before moving forward to the next processing step.

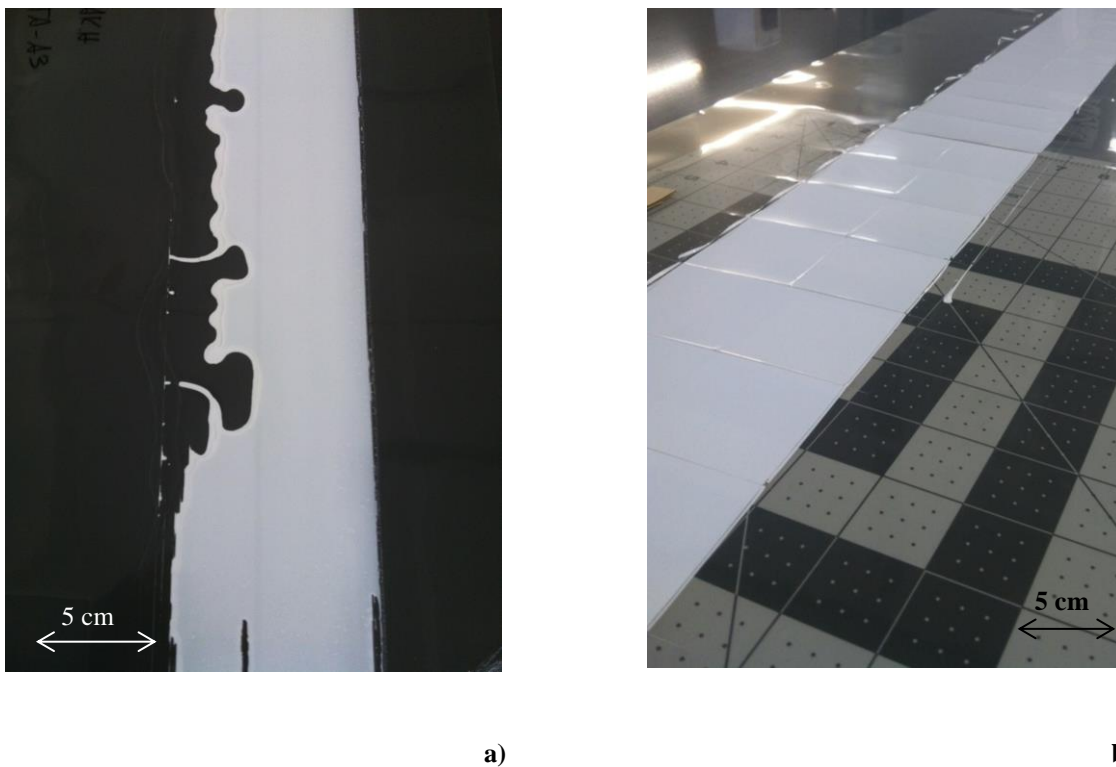


**Figure 9:** a) shows a non-wetted tape; b) a well wetted tape on the non silicon coated side cut into the required dimensions is seen

### *Cutting:*

The next step of the fabrication process was to cut the tape, which had a length of about 1.50 m, a width of 11 cm and a thickness of 60-75 $\mu$ m. The thickness variation depended on the viscosity of the slurry. The dimensions of cutting the final tape were 5x5 cm. Those cut layers were then stacked according to the required architecture of samples that were to be fabricated.

**Figure 10b)** shows a dry tape cut into the right dimensions.

### 2.2.6. Hot Pressing (HP) & Lamination (IP)

The next processing step is the hot pressing (HP) of the stacked layers, where the last layer on each side were kept as mylar material for the protection of the sample during pressing. The sample was put between two metallic tiles and hot pressed at a temperature of 75 °C at a pressure of 2 tons for 15 min.

After hot pressing, one of the metallic tiles was removed and a fitting rubber piece was put on top of the sample. This was then laminated and isostatically pressed at 75 °C (IP), a pressure of 20 MPa for 30 minutes.

These processing steps (HP&IP) were to form a compact sample and remove the air between the stacked layers.

### 2.2.7. Binder Burn Out (BB-Out)

As mentioned above the binder was added earlier to obtain a slurry with a good viscosity and a good handling of the tape. Otherwise without a binder the tape would break apart immediately. However, after the green state, the binder has to be removed (if possibly to 100%).

The processes of binder burn out were different depending on the binder system that was used. In general, the process for the removal of the organic components was divided into several steps with different temperatures and dwelling times.

#### *Binder Burn Out for the Acrylic binder system:*

First, after setting the ceramic sample on a porous ceramic holder into the furnace, it was heated with a rate of 0.2 °C/min to a temperature of 350 °C, where it was dwelled for 9 h.

In this step the plasticizer was removed, which had the lowest boiling temperature of the organic components.

For the second step the temperature was increased to 450 °C also with a rate of 0.2 °C/min and held for 4 h. Following the furnace was cooled down to room temperature with a rate of 1.6 °C/min, see **Fig. 11**.

At 450 °C all the other polymers were evaporated so that only an open pore ceramic structure was left over. It is important that the binder was totally removed, otherwise it could have happened that parts of the organic components got trapped in the ceramic structure due to the change of an open pore to a closed pore structure during sintering.

If polymers get trapped like this, they could cause cracking of the ceramic sample while evaporating during sintering at higher temperatures than during binder burn out. After binder burn out the sample was very brittle, therefore caution had to be taken at handling the material after this processing step.

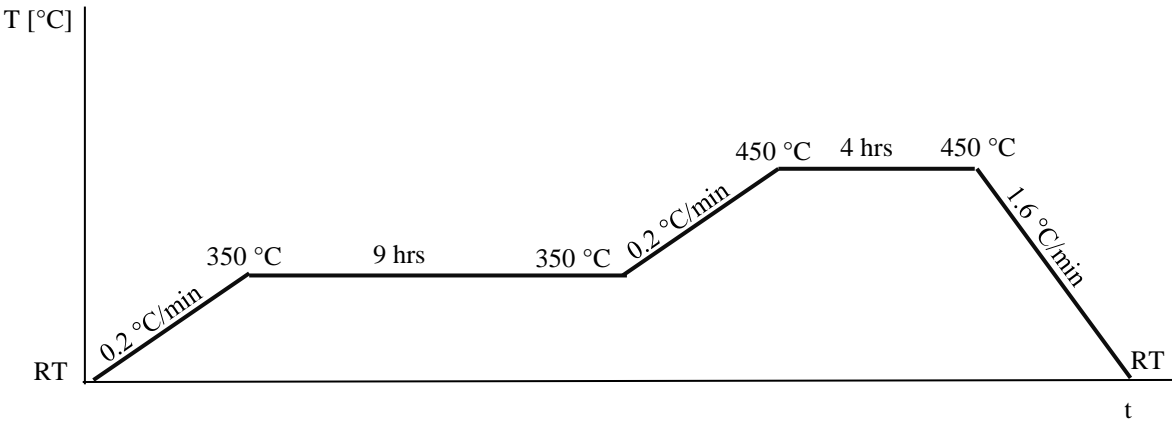


**Figure 11:** Diagram of the Binder Burn Out process for the Acrylic binder system

*Binder Burn Out for PVA binder system:*

For the PVA binder system a similar process as described above for the Acrylic binder system was followed, see **Fig. 12**.

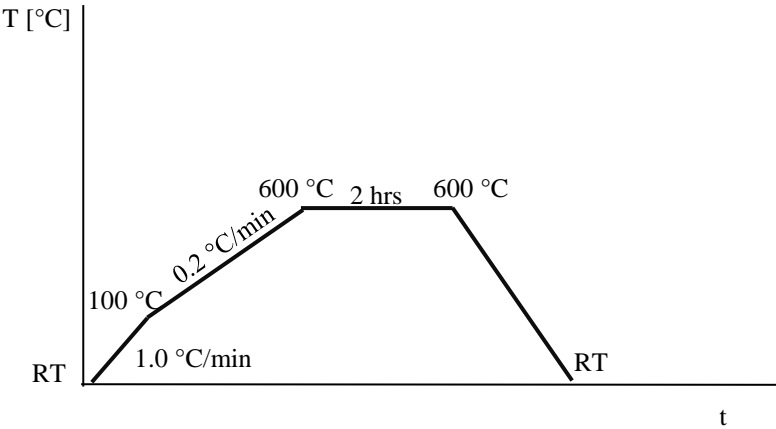


**Figure 12:** Diagram of the Binder Burn Out process for the PVA binder system

### 2.2.8. Cold Isostatic Pressing

Cold isostatic pressing (CIP) was applied to compress the ceramic sample after binder burn out to achieve a high density (~99%) after sintering. For the CIP the sample was vacuum sealed in two latex gloves and then cold isostatically pressed at 200 MPa.

### 2.2.9. Sintering

Sintering is the final step in the processing of a ceramic sample and can be described in three different stages, the Initial, the Intermediate and the Final stage.

#### *Initial stage:*

Here rearrangement of the particles occurs due to capillary forces, which results in an increase of the relative density (<75%) due to the increase of contacts between the single particles. In the area where the particles touch each other necks are formed via diffusion of atoms from either the surface or the inside of the ceramic particle.

#### *Intermediate stage:*

Through diffusion material deposits more and more in the necks between the particles, resulting in a continuous pore channel network. Additionally atoms diffuse from the neck towards the pores and reduce the amount of vacancies. In this stage a relative density of 75-92% can be reached.

#### *Final stage:*

Material that diffused towards the pore channels closes up the space and forms spherical pores. Due to the small size of the pores it is now easier for the grain boundaries to move. As a result pores get isolated on triple points, shrink and are removed via diffusion. In this stage also grain growth occurs which is driven by the force of reducing the surface energy between two grains having different crystallographic orientations. Usually grain growth can be observed at relative densities from 92-95%, where no interconnected pore network is still present. In the final stage a relative density of 99% can be achieved. [36]

As mentioned in the three stages of sintering, diffusion is responsible for the reduction of the ratio of pores and the formation of a dense, continuous microstructure. During sintering several different mechanisms of diffusion can be observed, which can be divided in non-densifying and densifying mechanisms.

The source for non-densifying mechanisms is the particle surface. From the surface of the particle the material diffuses either along the surface towards the contact between two particles (neck), or through the lattice or via vapor transport, see **Tab. 4** and **Fig. 13**.

For the densifying mechanisms the source can either be the boundary between two particles as a result from the neck formation or dislocations in the particles. The diffusion of atoms from the boundary can occur via diffusion along the boundary on the one hand and via lattice diffusion on the other hand. In comparison to that, the diffusion of material from a dislocation in the particle can only be observed via the lattice, see **Tab. 3** and **Fig. 13**.

**Table 4:** Sintering mechanisms [36]

mechanism	Transport path	Source	Sink
Non-Densifying			
1	Surface diffusion	Surface	Neck
2	Lattice diffusion	Surface	Neck
3	Vapour transport	Surface	Neck
Densifying			
4	Boundary diffusion	Boundary	Neck
5	Lattice diffusion	Boundary	Neck
6	Lattice diffusion	dislocations	Neck

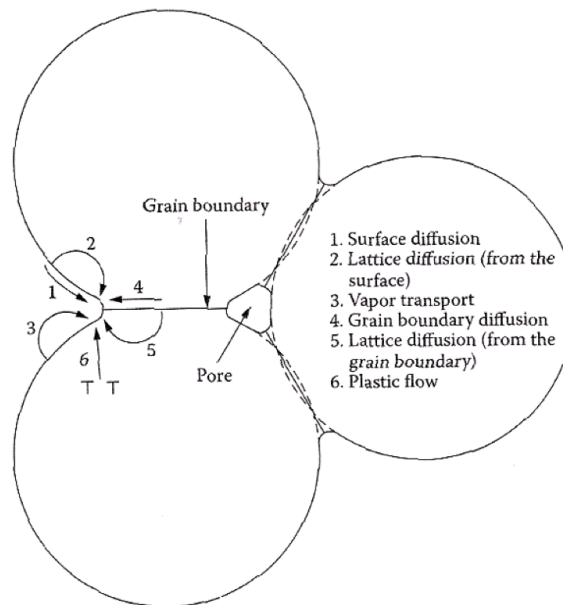


**Figure 13:** Schematic of the occurring diffusion mechanisms during sintering [36]

As mentioned in the preparation of the slurries, for the textured materials dopants were added to obtain liquid phase sintering. The presence of a liquid phase makes it possible to sinter at lower temperatures, because material dissolves into the liquid and can be transported to the required position much easier. This is important for templated grain growth, where it is wanted that material moves to the templates to increase their dimensions according to their orientations. The sintering of all the samples was carried out in a high temperature furnace at a temperature of 1550 °C. For the final processing step the part was placed on a crucible covered with tabular alumina and put into the furnace. This was heated with a rate of 5 °C/min up to 1550 °C and dwelled for 4 h, see **Fig. 14**.

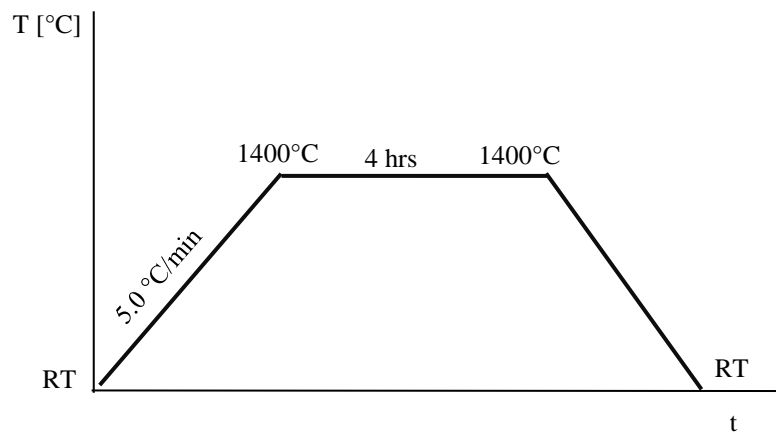


**Figure 14:** Diagram of the Sintering process

### 3. Results and discussion

#### 3.1. Selection of binder system

The first attempts to obtain a stable suspension were performed with the PVA binder system, which had been usually employed in formulating ceramic slurries. However, flocculation occurred during combining the binder system with the ceramic powder. These occurring flocs made the fabricated slurry impractical for further processing steps, and would have negatively influenced the aim of high density and a constant microstructure. Based upon this observation, different experiments were made. The order of adding components was changed, measurements of the pH were run and the PVA was dissolved in the DI-H<sub>2</sub>O at different temperatures. After not achieving any success it was considered that, since the PVA is an organic material, there is a possibility that microorganisms grow and pollute the binder material, which can lead to flocculation [37], dissolved in deionized water (DI-water) and mixed with the other organic

components (plasticizer, dispersant and defoamer). This solution was then diluted with a high amount of DI-water and filtered with an 1  $\mu\text{m}$  filter paper. After adding the ceramic powder and evaporating the DI-water, which was previously added to lower the viscosity of the solution and being able to filter it, no flocculation occurred.

Nevertheless, it was unsure how much of the organic components were lost through the filtering step and how this loss might affect the resulting samples. In addition to that, sintered samples fabricated with the Acrylic binder system showed a much higher relative density than the samples where the PVA binder system was used. Therefore, the Acrylic binder system was finally chosen for the stabilization of the slurries and further fabrication of all materials and architectures.

### 3.2. Dimensions and shrinkage of monolithic and layered samples

In order to determine the shrinkage of the materials, sample dimensions as indicated in **Figure 15** were measured during the different processing steps. **Table 5** displays the average values for the dimension measurements of the variety of non-textured, textured and laminated samples.



**Figure 15:** Measured dimensions

**Table 5:** Datas of dimension measurements and shrinkage calculations

material	dimensions	a <sub>1</sub>	$\Delta a_1(a_x - a_0)$		a <sub>2</sub>	$\Delta a_2(a_x - a_0)$		h	$\Delta h(h_x - h_0)$	
		[mm]	[mm]	[%]	[mm]	[mm]	[%]	[mm]	[mm]	[%]
TA	HP/IP	50.32			50.70			3.88		
	after BB-Out	50.44	0.12	0.23	50.55	-0.15	-0.30	3.78	-0.10	-2.61
	after CIP/sintering	44.19	-6.25	-12.38	44.43	-6.13	-12.12	3.02	-0.77	-20.26
	total shrinkage		-6.13	-12.18		-6.28	-12.38		-0.87	-22.35
material	dimensions	a <sub>1</sub>	$\Delta a_1(a_x - a_0)$		a <sub>2</sub>	$\Delta a_2(a_x - a_0)$		h	$\Delta h(h_x - h_0)$	
		[mm]	[mm]	[%]	[mm]	[mm]	[%]	[mm]	[mm]	[%]
EA	HP/IP	50.54			50.62			3.80		
	after BB-Out	50.47	-0.07	-0.13	50.69	0.06	0.13	3.77	-0.03	-0.88
	after CIP/sintering	41.52	-8.95	-17.74	41.33	-9.36	-18.46	3.07	-0.70	-18.48
	total shrinkage		-9.02	-17.85		-9.30	-18.36		-0.73	-19.19
material	dimensions	a <sub>1</sub>	$\Delta a_1(a_x - a_0)$		a <sub>2</sub>	$\Delta a_2(a_x - a_0)$		h	$\Delta h(h_x - h_0)$	
		[mm]	[mm]	[%]	[mm]	[mm]	[%]	[mm]	[mm]	[%]
P	HP/IP	50.45			50.34			2.79		
	after BB-Out	50.25	-0.20	-0.39	49.91	-0.43	-0.85	2.82	0.04	1.35
	after CIP/sintering	42.02	-8.24	-16.39	41.82	-8.08	-16.20	2.23	-0.59	-20.95
	total shrinkage		-8.44	-16.72		-8.51	-16.92		-0.55	-19.88
material	dimensions	a <sub>1</sub>	$\Delta a_1(a_x - a_0)$		a <sub>2</sub>	$\Delta a_2(a_x - a_0)$		h	$\Delta h(h_x - h_0)$	
		[mm]	[mm]	[%]	[mm]	[mm]	[%]	[mm]	[mm]	[%]
NP1	HP/IP	50.24			50.18			3.12		
	after BB-Out	50.00	-0.24	-0.47	49.94	-0.24	-0.49	3.07	-0.05	-1.60
	after CIP/sintering	41.65	-8.35	-16.70	41.56	-8.38	-16.79	2.41	-0.66	-21.52
	total shrinkage		-8.58	-17.09		8.63	-17.19		-0.71	-22.78

material	dimensions	a <sub>1</sub>	Δa <sub>1</sub> (a <sub>x</sub> -a <sub>0</sub> )		a <sub>2</sub>	Δa <sub>2</sub> (a <sub>x</sub> -a <sub>0</sub> )		h	Δh(h <sub>x</sub> -h <sub>0</sub> )	
		[mm]	[mm]	[%]	[mm]	[mm]	[%]	[mm]	[mm]	[%]
NP2	HP/IP	50.18			50.27			4.23		
	after BB-Out	49.96	-0.22	-0.44	49.98	-0.30	-3.76	4.07	-0.16	-3.76
	after CIP/sintering	41.59	-8.37	-16.75	41.70	-8.27	-13.15	3.53	-0.54	-13.15
	total shrinkage		-8.59	-17.12		-8.57	-16.42		-0.69	-16.42

### 3.3. Density measurements

For density measurements the Archimedes method was used. Depending on whether the material measured is porous or dense different weights have to be taken in account. Whereas for dense materials the sample is only weighed dry and in liquid, materials containing pores also have to be weighed in air when they are saturated with liquid.

The liquid used for the density measurements was DI-H<sub>2</sub>O having a density (ρ<sub>l</sub>) of 1 g/cm<sup>3</sup>. Porous materials are defined to have an open porosity resulting in a relative density <95%. For density calculations equation (1) was applied. [36]

$$\rho_b = \frac{m_d \times \rho_l}{(m_s - m_l)} \quad [\text{g/cm}^3] \quad (1)$$

m<sub>d</sub> - mass of dry sample measured in air [g]

m<sub>l</sub> - mass of sample suspended in liquid [g]

m<sub>s</sub> - mass of sample saturated with liquid measured in air [g]

To receive the relative density (ρ<sub>rel</sub>), the calculated bulk density (ρ<sub>b</sub>) of the material has to be divided by the theoretical density (ρ<sub>th</sub>), see equation (2).

$$\rho_{rel} = \frac{\rho_b}{\rho_{th}} \times 100 \quad [\%] \quad (2)$$

The theoretical density for alumina (ρ<sub>th</sub>(Al<sub>2</sub>O<sub>3</sub>) [30]) is 3.986 g/cm<sup>3</sup>, and for zirconia ρ<sub>th</sub>(ZrO<sub>2</sub>)=5.680 g/cm<sup>3</sup> [32]. For the non-textured material the theoretical density was calculated as a combination of the theoretical densities of alumina and zirconia, due to the composition of 95% alumina and 5% zirconia. Accordingly the theoretical density for the non-textured material (ρ<sub>th</sub>(Al<sub>2</sub>O<sub>3</sub>+ZrO<sub>2</sub>)) was 4.071 g/cm<sup>3</sup>.

**Table 6** shows the average values of the density measurements and the calculated densities and relative densities through equ. (1) and (2), respectively, for the textured (TA) and non-textured (EA) monolithic samples.

**Table 6:** datas of measured masses and of density calculations [30,32]

material	# of considered samples	$m_d$	$m_l$	$m_s$	$\rho_b$	$\rho_{th}$	$\rho_{rel}$
		[g]	[g]	[g]	[g/cm <sup>3</sup> ]	[g/cm <sup>3</sup> ]	[%]
TA	5	20.4324	15.1748	20.5093	3.830	3.986	96.09
EA	6	20.1463	15.1766	20.1758	4.030	4.071	99.00

### 3.4. Microstructural characterization

For the microstructural characterization of the samples optical and scanning electron microscopy (SEM) was conducted. Furthermore, to determine the degree of orientation in textured samples, X-Ray diffraction was applied and the Lotgering defined, according to equation (3).

#### 3.4.1. Sample preparation

For the microscopic analysis samples had to be prepared.

First samples were cut into dimensions no bigger than 10x10x3 mm to fit into the chamber of the SEM. For the cutting a high speed cutting machine (speed ~2000 rpm) and a diamond coated blade were used.

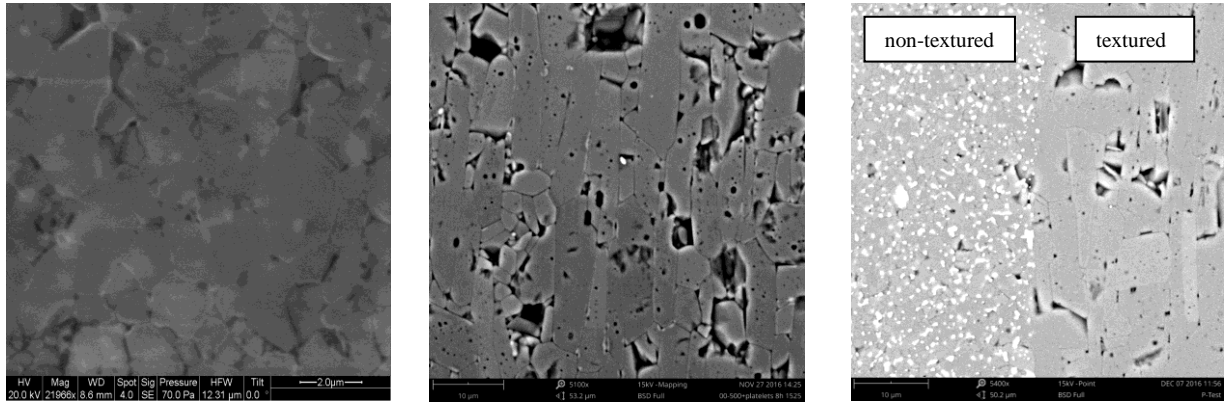
Following the cut parts were grinded with a disk with a grade of 10  $\mu\text{m}$  for about 10 min. After grinding all the samples were polished at three different grades for approximately 30 min, starting with 6  $\mu\text{m}$ , then 3  $\mu\text{m}$  and finally a grade of 1  $\mu\text{m}$ .

Between the particular steps and after the polishing the sample was put into DI-H<sub>2</sub>O and cleaned in an ultra-sonic device.

#### 3.4.2. Optical and scanning electron microscopy (SEM)

**Figure 16** shows three images taken with a scanning electron microscope (Model Quanta 200, FEI, Hillsboro, OR, USA). Fig. 16a) displays a microstructure of an equiaxed material, where the grain size is about 1  $\mu\text{m}$ . In comparison to that, in Fig. 16b), which shows textured alumina, the grains have a high aspect ratio, where grains have an estimated length of 15-20  $\mu\text{m}$  and a width of 5  $\mu\text{m}$ .

Additionally Fig. 16c) presents an interface between the two different materials, non-textured and textured.



a)

b)

c)

**Figure 16:** SEM pictures of the microstructure of a) equiaxed alumina, b) textured alumina and c) an interface of equiaxed and textured alumina

In order to measure the thickness of the sintered samples, an optical microscope (Model BX50, Olympus, Shinjuku, Tokyo, Japan) was employed. Results are listed in **Tab. 7**, corresponding to the individual layers in **Fig.17**.



a)

b)

c)

**Figure 17:** Optical Microscope pictures of layered architectures: a) periodic, b) non-periodic: design 1, c) non-periodic: design 2

**Table 7:** list of desired and actual thickness of the layers in the laminated samples

		#	Desired thickness of layer	Actual thickness of layer
			[ $\mu\text{m}$ ]	[ $\mu\text{m}$ ]
Periodic	layer	1	360	327
		2	75	93
		3	360	294
		4	75	119
		5	360	320
		6	75	116
		7	360	325
		8	75	129
		9	360	319
Non-periodic 1	layer	1	50	42
		2	150	153
		3	1700	1606
		4	150	144
		5	50	49
Non-periodic 2	layer	1	50	43
		2	250	311
		3	2900	2695
		4	250	398
		5	50	52

<sup>†</sup>a factor for the variations of the desired thicknesses compared to the actual thicknesses can be the variation of the thicknesses of the fabricated tapes, due to the not automated process

### 3.4.3. Degree of texture through X-Ray analysis

During templated grain growth grains the basal plane (0001) of the hexagonal crystal structure is oriented parallel to the surface of a sample, perpendicular to the c-axis in the crystal, see hexagonal crystal structure in **Fig. 18**. How well textured the samples were, could be analyzed via X-Ray diffraction. X-Ray diffraction patterns show two very significant in two of the (000z) directions ((0006) and (000 12)) in textured alumina, whereas in a randomly oriented alumina those peaks are hardly remarkable, see X-Ray pattern in **Fig. 19a**). As a result of the height of

these two peaks it can be determined how high the degree of orientation is in the textured material, which is described by the so-called Lotgering factor (LF).

$$LF = \frac{p-p_0}{1-p_0} \quad (3)$$

$$p = \frac{\text{textured peaks of textured sample}}{\text{sum of all peaks of textured sample}}$$

$$p_0 = \frac{\text{textured peaks of random sample}}{\text{sum of all peaks of random sample}}$$

For the calculation of the Lotgering factor a XRD-pattern of a randomly oriented pure alumina was taken as well, see **Fig. 19b**). As already mentioned the LF gives states the degree of orientation in a textured material, meaning the higher LF, the better the orientation of the grain perpendicular to the c-axis. **Table 8** shows the calculated LFs for the fabricated textured samples in this study.

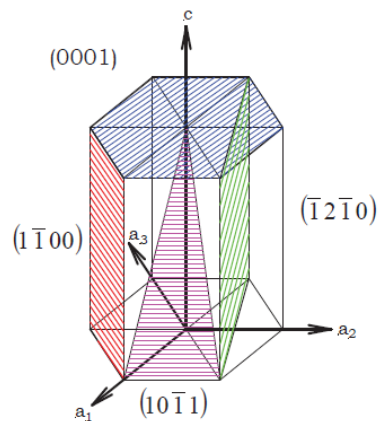
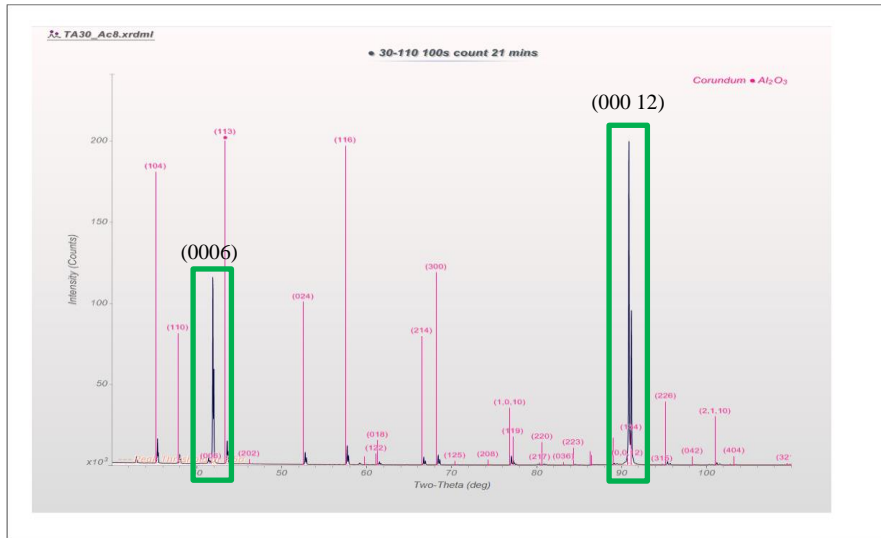
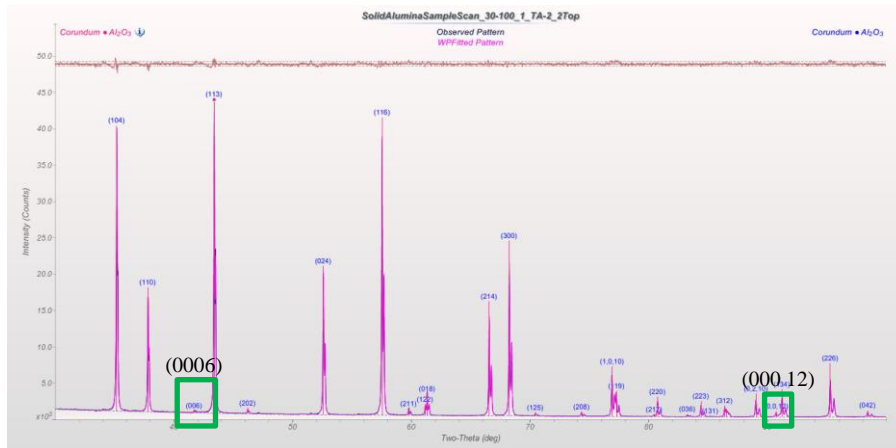


**Figure 18:** hexagonal crystal structure showing the (0001) plane [38]



a)



b)

**Figure 19:** XRD diffraction patterns of a) textured and b) randomly oriented alumina

**Table 8:** Lotgering factors of fabricated textured alumina samples

sample	#	LF
		[%]
TA30-Ac2,3	1	43.62
TA30-Ac4_1	2	66.00
TA30-Ac4_2	3	71.78
TA30-Ac6	4	41.60
TA30-Ac8	5	71.65

## 4. Future work

The samples fabricated in the laboratories of Penn State University during this research period are planned to be characterized at the Institute for Structural and Functional Ceramics at the Montanuniversität Leoben. .

Physical properties such as Young's Modulus ( $E$ ) and Coefficient of Thermal Expansion (CTE) will be determined in textured and non-textured monolithic samples. The mechanical characterization will include the evaluation of the critical stress intensity factor ( $K_{IC}$ ) and the flexural strength on both monoliths (textured and non-textured materials) and laminates (periodic and non-periodic architectures).

The main focus will be set on assessing the effect of the different layered architectures with textured and non-textured microstructures on the crack growth resistance behavior. Recent work of the team has demonstrated that the combination of textured layers and compressive stresses significantly increases the apparent fracture toughness in a periodic layered structure features [28]. Fracture process begins with crack arrest at the compressive (textured) layer, followed by delamination of the platelets in the textured layer (see **Fig. 20**).

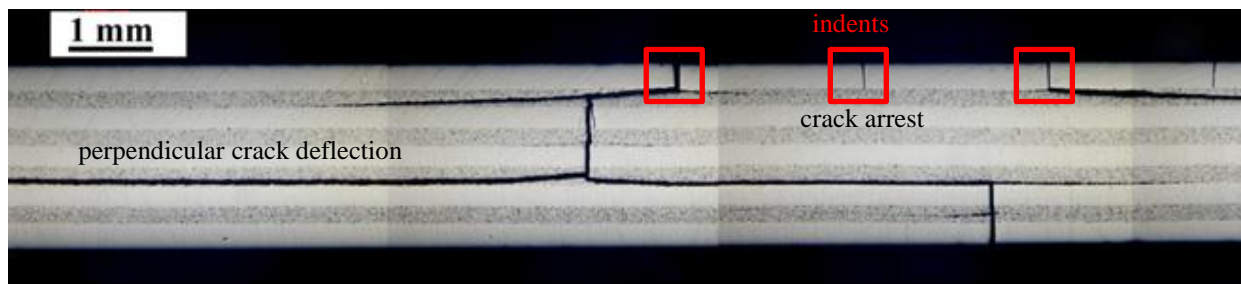


**Figure 20:** crack arrest and deflection perpendicular to the applied stress direction [28]

The combination of textured compressive layers in a “non-periodic” architecture, as it has been fabricated in this research work, is hypothesized to reach unprecedented toughness values for ceramic materials, as well as guaranteeing a relatively high minimum strength.

This behavior can be tailored by adjusting the residual stresses ( $\sigma_{res}$ ) in the layers, which occur (for instance) due to the different coefficients of thermal expansion of the two combined materials (in our case textured and non-textured composites). The aim is to tailor the compressive residual stresses in the second (textured) layer in order to improve the apparent fracture toughness of the material, as given by the following equation:

$$K_R(a) = K_{Ic} - \int_0^a h(a, x) \times \sigma_{res} dx \quad (4)$$

Where  $K_R(a)$  is the apparent fracture toughness as a function of the crack length ( $a$ ),  $h(a,x)$  is the so-called weight function (taking into account the geometry of the sample and crack and loading configuration),  $\sigma_{res}$  is the in-plane compressive/tensile residual stress in the corresponding layer and  $K_{Ic}$  is the critical stress intensity factor (fracture toughness) of the corresponding layer.

This model has been previously derived by the team for periodic and non-periodic (non-textured) architectures, as shown in **Figure 21**. It is shown how  $K_R$  first decreases, when the crack propagates through the outer most (tensile) layer. When the crack reaches the interface of the two different materials, in this study non-textured and textured,  $K_R$  increases remarkably. So far this curve is a model that has been proven experimentally on textured periodic architectures, and now it should be extended to textured non-periodic designs, as fabricated in this research work.

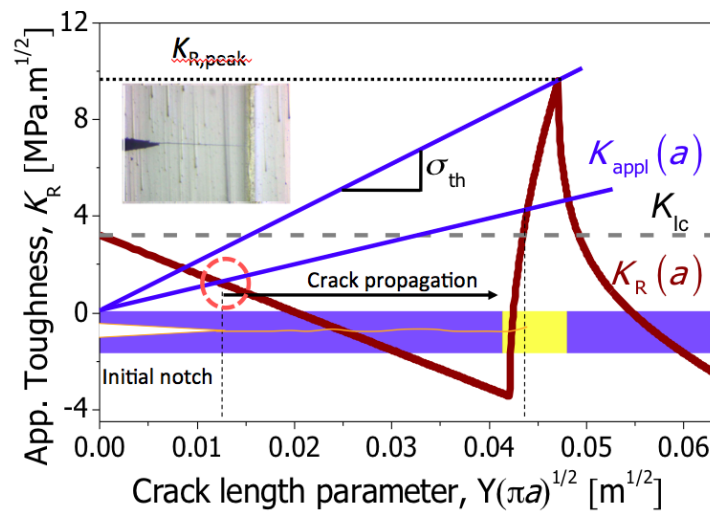


**Figure 21:** Model of the apparent fracture toughness in a multilayer compound [28]

## References

- [1] R. Morrell, *Fractography of Brittle Materials*, National Physical Laboratory, Teddington, 1999.
- [2] R. Danzer, *Key Eng. Mat.*, 223 (2002) 1-18.
- [3] D. Munz, T. Fett, *Ceramics. Mechanical Properties, Failure Behaviour, Materials Selection*, Springer, Berlin, 1999.
- [4] R. Danzer, T. Lube, P. Supancic, R. Damani, *Adv. Eng. Mat.*, 10 (2008) 275-298.
- [5] A. Roosen, Tape casting of ceramic green tapes for multilayer device processing, in: H.J. Jean, T.K. Gupta, K.M. Nair, K. Niwa (Eds.) *Ceramic Transactions*, The American Ceramics Society, Columbus, Ohio, 1999.
- [6] A. Roosen, *J. Eur. Ceram. Soc.*, 21 (2001) 1993-1996.
- [7] F.F. Lange, *J. Am. Ceram. Soc.*, 72 (1989) 3-15.
- [8] A.G. Evans, *J. Am. Ceram. Soc.*, 73 (1990) 187-206.
- [9] P.F. Becher, *J. Am. Ceram. Soc.*, 74 (1991) 255-269.
- [10] M.P. Harmer, H.M. Chan, G.A. Miller, *J. Am. Ceram. Soc.*, 75 (1992) 1715-1728.
- [11] G.L. Messing, S. Trolier-McKinstry, E.M. Sabolsky, C. Duran, S. Kwon, B. Brahmaroutu, P. Park, H. Yilmaz, P.W. Rehrig, K.B. Eitel, E. Suvaci, M. Seabaugh, K.S. Oh, *Critical Reviews Solid. Stat. Mater. Sci.*, 29 (2004) 45–96.
- [12] M.M. Seabaugh, I.H. Kerscht, G.L. Messing, *J. Am. Ceram. Soc.*, 80 (1997) 1181-1188.
- [13] R.J. Pavlacka, G.L. Messing, *J. Eur. Ceram. Soc.*, 30 (2010) 2917-2925.
- [14] E. Suvaci, G.L. Messing, *J. Am. Ceram. Soc.*, 83 (2000) 2041-2048.
- [15] W.J. Clegg, K. Kendall, N.M. Alford, T.W. Button, J.D. Birchall, *Nature*, 347 (1990) 455-457.
- [16] D.B. Marshall, J.J. Ratto, F. Lange, *J. Am. Ceram. Soc.*, 74 (1991) 2979-2987.
- [17] R. Lakshminarayanan, D.K. Shetty, R.A. Cutler, *J. Am. Ceram. Soc.*, 79 (1996) 79-87.
- [18] J. Sanchez-Herencia, J. Moya, A. Tomsia, *Scripta Mater.*, 38 (1998) 1-5.
- [19] M. Rao, J. Sanchez-Herencia, G. Beltz, R.M. McMeeking, F. Lange, *Science*, 286 (1999) 102-105.
- [20] M.G. Pontin, M. Rao, J. Sanchez-Herencia, F. Lange, *J. Am. Ceram. Soc.*, 85 (2002) 3041-3048.
- [21] R.J. Moon, M. Hoffman, J. Hilden, K.J. Bowman, K.P. Trumble, J. Rödel, *Eng. Fract. Mech.*, 69 (2002) 1647-1665.

- [22] M. Lugovy, V. Slyunyayev, V. Subbotin, N. Orlovskaya, G. Gogotsi, *Composite Science and Technology*, 64 (2004) 1947-1957.
- [23] V.M. Sglavo, M. Paternoster, M. Bertoldi, *J. Am. Ceram. Soc.*, 88 (2005) 2826-2832.
- [24] R. Bermejo, C. Baudín, R. Moreno, L. Llanes, A.J. Sánchez-Herencia, *Composite Science and Technology; Comp. Sci. Tech.*, 67 (2007) 1930-1938.
- [25] R. Bermejo, Y. Torres, C. Baudin, A.J. Sánchez-Herencia, J. Pascual, M. Anglada, L. Llanes, *J. Eur. Ceram. Soc.*, 27 (2007) 1443-1448.
- [26] R. Bermejo, J. Pascual, T. Lube, R. Danzer, *J. Eur. Ceram. Soc.*, 28 (2008) 1575-1583.
- [27] R. Bermejo, C. Baudin, R. Moreno, L. Llanes, A.J. Sanchez-Herencia, *Comp. Sci. Tech.*, 67 (2007) 1930-1938.
- [28] Y. Chang, R. Bermejo, G.L. Messing, *J. Am. Ceram. Soc.*, 97 (2014) 3643-3651.
- [29] R. Bermejo, L. Ceseracciu, L. Llanes, M. Anglada, *Key Eng. Mat.* 409 (2009) 94-106.
- [30] E.Dörre, H.Hübner, *Materials Research and Engineering*, Springer Verlag, (1984)
- [31] [https://upload.wikimedia.org/wikipedia/commons/thumb/a/a5/-Corundum\\_struct.png/300px-Corundum\\_struct.png](https://upload.wikimedia.org/wikipedia/commons/thumb/a/a5/-Corundum_struct.png/300px-Corundum_struct.png) on 03/18/2017
- [32] H.Salmang, H.Scholze, *Keramik*, Springer Verlag, (2007)
- [33] <https://upload.wikimedia.org/wikipedia/commons/0/00/YSZ.jpg> on 03/18/2017
- [34] R.Bermejo, *Doctoral Thesis*, Universitat Politecnica de Catalunya, (2006)
- [35] F.F. Lange, *J. Am. Ceram. Soc.*, 72, (1989) 3-15.
- [36] Information from taken lecture at PSU, “Ceramic Processing”, MatSE 411, G.L.Messing, (2016)
- [37] R.A.Terpstra, P.Pex, A.deVries, “Ceramic Processing”, Springer Verlag, (1995)
- [38] Information from taken lecture at MUL, “Structure and Scattering Methods”, 430.020, J.Keckes